Scaling Laws for Three-Dimensional Combined Heaving and Pitching Propulsors

Fatma Ayancik,* Amin Mivehchi,† and Keith W. Moored‡
Lehigh University, Bethlehem, Pennsylvania 18015

https://doi.org/10.2514/1.J060482

We present three-dimensional scaling relations for the thrust production and power consumption of combined heaving and pitching hydrofoils by extending the three-dimensional pitching scaling laws introduced by Ayancik et al. ("Scaling Laws for the Propulsive Performance of Three-Dimensional Pitching Propulsors," *Journal of Fluid Mechanics*, Vol. 871, July 2019, pp. 1117–1138). Self-propelled inviscid simulations and previously published experimental data are used to validate the scaling laws over a wide range of motion amplitudes, Strouhal numbers, heave ratios, aspect ratios, and pitch axis locations. The scaling laws are shown to predict inviscid numerical and experimental data well, within ±25% and ±16% of the thrust and power data, respectively. It reveals that both the circulatory and added mass forces are important when considering a wide range of motion amplitudes and that nonlinear corrections to the classic linear theory are essential to modeling the power performance across a wide amplitude and aspect ratio range. By using the scaling laws as a tool, it is obtained that peak efficiency occurs when dimensionless amplitude $A^* > 1$ and for these large-amplitude motions there is an optimal nondimensional heave ratio h^*, where the efficiency maximizes in the narrow range of $0.75 < h^* < 0.94$. Finally, the scaling laws show that to further improve efficiency in this high-efficiency regime, the aspect ratio and dimensionless amplitude should be increased, whereas the Lighthill number should be decreased (lower drag and/or a larger propulsor planform area to wetted surface area ratio), and the pitch axis should be located behind the leading edge. This scaling model can be used to guide the design of the next generation of high-efficiency bio-inspired machines.

Nomenclature

A	=	total peak-to-peak amplitude of the trailing edge, m
$\mathcal{AR}$	=	aspect ratio
a	=	pitch axis location
c	=	chord length, m
C_D	=	drag coefficient
C_P	=	pressure coefficient
C_T	=	thrust coefficient
f	=	frequency, Hz
h_0	=	heave amplitude, m
Li	=	Lighthill number
m	=	mass, kg
S_p	=	planform area, m^2
S_w	=	wetted surface area, m^2
U	=	swimming speed, m/s
η	=	efficiency
θ_0	=	pitch amplitude, deg
ρ	=	density

Subscripts

TE	=	trailing edge
sep	=	separating shear layer
prox	=	vortex proximity

Superscripts

dyn	=	dynamic pressure scaled
net	=	net force

Received 24 February 2021; revision received 8 October 2021; accepted for publication 23 December 2021; published online 16 February 2022.

*Ph.D. Student, Department of Mechanical Engineering.
†Postdoctoral Researcher, Department of Mechanical Engineering.
‡Associate Professor, Department of Mechanical Engineering.

I. Introduction

THE engineering of fast, efficient, maneuverable, and quiet bio-inspired propulsive systems has spurred scientific interest in recent years into investigating the unsteady hydrodynamics of fish swimming. Researchers have specified the complex flow features that are correlated with efficient thrust production [1–10], revealing that an essential pursuit is a deeper understanding of the origins of unsteady hydrodynamic forces. In this context, some researchers have reduced these flow phenomena into scaling relations under net-thrust and fixed-velocity conditions [11–16], or for self-propelled organisms [17].

The basis of many recent scaling laws lies in classic unsteady linear theory. The theories of [18–20] have become particularly useful in this pursuit due to their clear assumptions (incompressible and inviscid flow, small-amplitude motions, nondeforming and planar wakes) and the identification of the physical origins of their terms. For instance, these theories decompose the forces acting on unsteady foils into three types: added mass, quasi-steady, and wake-induced forces. Theodorsen's theory was extended by Garrick [19] by accounting for the singularity in the vorticity distribution at the leading edge to determine the thrust force produced and the power required by such motions [21]. By following, [13–15,19] nondimensionalized the thrust forces of heaving and pitching flexible panels with their added mass forces. Moored and Quinn [22] advanced this previous work by considering both the added mass and the circulatory forces of self-propelled pitching foils, as well as wake-induced nonlinearities that are not considered in classical linear theory [19]. It was shown that data generated from a potential flow solver was in excellent agreement with the proposed scaling laws. Similarly, Floryan et al. [23] considered both the circulatory and added mass forces in their scaling laws and showed excellent collapse of experimental data for the thrust and power forces of a rigid two-dimensional heaving or pitching foil. Following that work, Van Buren et al. [24] developed scaling relations for two-dimensional foils undergoing combined heaving and pitching motions. Even though existing studies have offered extensive insights into the origins of unsteady force production, they have been limited to two-dimensional propulsors.

The scaling laws proposed by [22] were extended to three-dimensional pitching propulsors [25] of various aspect ratios by accounting for the added mass of a finite-span propulsor, the

downwash/upwash effects from the trailing vortex system, and the elliptical topology of shedding trailing-edge vortices. It was demonstrated that the previous two-dimensional scaling laws as well as their three-dimensional enhancement collapsed both potential flow numerical data as well as experimental data. Later, [26] developed scaling relations for self-propelled three-dimensional cetacean propulsors undergoing *large-amplitude* combined heaving and pitching motions, which were verified through the use of potential flow numerical data. By using these scaling laws as a guide, it was demonstrated that the added mass forces played an essential role in understanding the variation in the efficiency with aspect ratio, however, circulatory forces play the predominant role in understanding the variation in the thrust and power with aspect ratio.

Here, we advance the scaling relations introduced in [25,26] to develop new scaling laws for three-dimensional combined heaving and pitching propulsors valid over a *wide range of amplitude and aspect ratio* and verified with both numerical and experimental data. In the article, Sec. II details the problem formulation, input, and output variables of the current study. Section III describes the numerical methodology, gives details about the boundary element method, and briefly describes the methodology of the previously published experimental data used to verify the scaling laws. Section IV outlines the development of the scaling laws. Section V presents the verification of the scaling laws through new potential flow numerical simulations and previously published experimental data. Finally, Sec. VII analyzes the scaling laws to derive physical insights for bio-inspired locomotion.

II. Problem Formulation

The developed scaling laws are verified with new simulations and previous experiments from literature. The numerical data are collected for an idealized self-propelled inviscid swimmer, where its velocity is an output of the imposed kinematics and interaction with the fluid environment. There is a lack of similar self-propelled experimental data in literature, however, towed and imposed-velocity water channel experimental data are available for three-dimensional combined heaving and pitching foils [25,27]. These experiments will be used to further verify that the proposed scaling laws also apply to viscous flows. Even though the simulations examine self-propelled foils and the experiments examine fixed-velocity foils the scaling laws should equally apply to both scenarios, as has been shown previously [22]. This equivalency occurs because the streamwise surging velocities of self-propelled swimming have been shown to have a negligible impact on the thrust and power of a foil [28]. Sections II.A–II.C will describe the *self-propelled* problem formulation, and its associated input and output variables. Section III.A will then describe the numerical methods used to solve the self-propelled problem, whereas Sec. III.B will briefly describe the fixed-velocity problem formulation and the experimental methodologies. Further details on the fixed-velocity problem formulation can be found in [25,27].

A. Idealized Self-Propelled Swimmer

An idealized swimmer is introduced to perform self-propelled simulations, as already addressed in [25]. The idealized swimmer is defined as an ensemble of a virtual body and a propulsor (Fig. 1). The three-dimensional propulsor undergoes combined heaving and pitching motions and has a rectangular planform shape, a NACA 0012 cross-sectional profile, and a chord length of $c = 0.1$ m. The propulsor planform area is $S_p = sc$, where s corresponds to the span length of the rectangular propulsor. The aspect ratio then becomes as $\mathcal{R} = s/c$, which is varied from 1 to 1000 in the current study. The highest aspect ratio value, $\mathcal{R} = 1000$, is chosen to represent a two-dimensional propulsor. A drag force D is applied to the propulsor, representing the effect of a virtual body that is not present in the computational domain. The drag force is determined by using a classic high Reynolds number drag law, in which drag varies proportionally with the square of the swimming speed U as

$$D = \frac{1}{2}\rho C_D S_w U^2 \tag{1}$$

where ρ is the density of fluid, C_D is the drag coefficient, and S_w corresponds to the total wetted surface area, which is calculated as the product of the propulsor planform area and the ratio of the wetted area to propulsor planform area S_{wp}. The area ratio is chosen to be 5, 10, and 15 in the current study.

B. Input Variables and Propulsor Kinematics of Self-Propelled Swimmer

Swimmers attain a cruising condition when the time-averaged drag and thrust are balanced in self-propelled locomotion [29]. How drag and thrust forces are balanced on a self-propelled swimmer can be represented by the Lighthill number $Li = C_D S_{wp}$, as a multiplication of area ratio and the drag coefficient. The Lighthill number represents the loading (thrust coefficient based on dynamic pressure) that occurs on the propulsor during self-propelled swimming. When the Li number is low there will be low propulsor loading and swimmers will typically attain faster swimming speeds than high-Li-number swimmers for a fixed set of kinematics and propulsor geometry [26]. In this study, by keeping the drag coefficient fixed to $C_D = 0.01$, which are typical values for cetaceans [30,31], the Lighthill number is changed from 0.05 to 0.15 by adjusting the area ratio. The dimensionless mass of the swimmer is determined as the ratio of body mass and a characteristic added mass of the propulsor, $m^* = m/\rho S_p c$, and is chosen to be 1.

The propulsor undergoes sinusoidal combined heaving and pitching motions about its pitching axis, where the heave and pitch motion are described as

$$h(t) = h_0 \sin(2\pi f t) \tag{2}$$

$$\theta(t) = \theta_0 \sin(2\pi f t + \psi) \tag{3}$$

where h_0 is the heave amplitude, f is the frequency, t is time, θ_0 is the pitching amplitude, and ψ is the phase angle between pitch and heave in radians and is chosen as $\psi = -\pi/2$, which is characteristic of biological locomotion [32]. The total peak-to-peak amplitude

$$A = A_{\mathrm{TE}}(t^*) = 2[h(t^*) + (c/2)(1 - a)\sin(\theta(t^*))] \tag{4}$$

depends upon both the heave and pitch motions and is defined when the trailing-edge amplitude reaches its maximum. This time is represented as t^*. The dimensionless pitching axis location is a, with

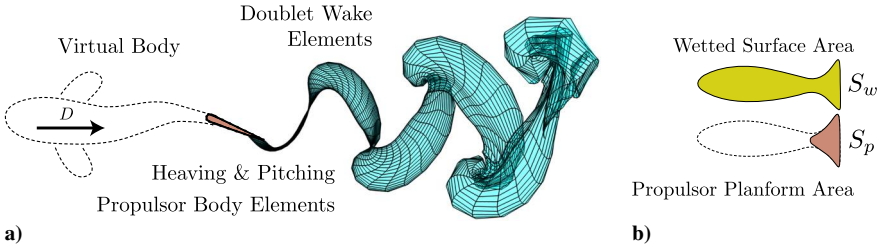

Fig. 1 a) Sketch of an idealized swimmer, and b) illustration of the propulsor planform and wetted surface area. (Reprinted with permission from Ayancik et al. [25]. Copyright 2019 by Cambridge University Press.)

Table 1 Input variables and parameters used in the current study

Computational input variables/parameters:	
Aspect ratio $\mathcal{AR}$	$1 \leq \mathcal{AR} \leq 1000$
Heave ratio (h^*)	$0.01 \leq h^* < 0.95$
Lighthill number (Li)	$0.05 \leq Li \leq 0.15$
Frequency (f) [Hz]	$f = 1$
Reynolds number (Re)	$Re \to \infty$
Experimental input variables/parameters:	
Tow tank [27,37]:	
Aspect ratio $\mathcal{AR}$	$\mathcal{AR} = 4.9$ and $\mathcal{AR} = \infty$
Heave ratio (h^*)	$0.82 < h^* < 1$
Frequency (f) [Hz]	$0.64 < f < 0.87$
Reynolds number (Re)	$Re = 21{,}000$
Closed-loop water channel [25]:	
Aspect ratio $\mathcal{AR}$	$\mathcal{AR} = 1.0, 1.5, 2$ and $\mathcal{AR} = \infty$
Heave ratio (h^*)	$h^* = 0$
Frequency (f) [Hz]	$0.5 \leq f \leq 2$
Reynolds number (Re)	$Re = 30{,}000$

$a = -1$ and 1 representing the leading- and trailing-edge locations, respectively. The dimensionless amplitude is then $A^* = A/c$. The proportion of the total amplitude that is derived from heaving is

$$h^* = 2h(t^*)/A \tag{5}$$

and the proportion derived from pitching is then

$$\theta^* = 1 - h^* \tag{6}$$

The heave ratio h^* is implicitly a heave-to-pitch ratio because it represents both the proportions of the heave and pitch to the total amplitude. For example, when $h^* = 1$ ($\theta^* = 0$) the motion is purely heaving, when $h^* = 0.5$ ($\theta^* = 0.5$) the motion is a perfect balance of heaving and pitching amplitudes, and when $h^* = 0$ ($\theta^* = 1$) the motion is purely pitching.

The input parameters of the study are listed in Table 1 for the numerical simulations and the experiments. For the new simulations, the range of frequency, amplitude, and aspect ratio are selected to obtain a data set that is characteristic to biological and bio-inspired propulsion [29,33] in terms of the Strouhal number, reduced frequency, and aspect ratio.

C. Output Variables of Self-Propelled Swimmer

All of the output variables are reported as mean quantities that are time-averaged over the last oscillation cycle and are indicated with an overline as $\bar{(\cdot)}$. All mean quantities are taken after a swimmer has reached quasi-steady-state swimming, defined as the time when the mean net thrust coefficient is $C_T^{\text{net}} \leq 10^{-5}$ that is defined as

$$C_T^{\text{net}} = \frac{(\bar{T} - \bar{D})}{(1/2)\rho S_p \bar{U}^2} \tag{7}$$

with T being the thrust force, obtained by integrating the $-x$ projection of the pressure forces over the surface of the hydrofoil. At this quasi-steady-state condition the time-averaged swimming speed is determined, and used to calculate the Strouhal number and the reduced frequency as

$$k = \frac{fc}{\bar{U}}, \qquad St = \frac{fA}{\bar{U}} \tag{8}$$

From the small amplitude theory [19], the added mass forces and added mass power are used to nondimensionalize the time-averaged thrust and power coefficients as

$$C_T = \frac{\bar{T}}{\rho S_p f^2 A^2}, \qquad C_P = \frac{\bar{P}}{\rho S_p f^2 A^2 \bar{U}} \tag{9}$$

Also, they can be scaled by the dynamic pressure,

$$C_T^{\text{dyn}} = \frac{\bar{T}}{(1/2)\rho S_p U^2}, \qquad C_P^{\text{dyn}} = \frac{\bar{P}}{(1/2)\rho S_p U^3} \tag{10}$$

By a simple transformation, the normalizations from the small amplitude theory and dynamic pressure can be related by $C_T^{\text{dyn}} = C_T(2St^2)$ and $C_P^{\text{dyn}} = C_P(2St^2)$.

III. Numerical and Experimental Methods

A. Unsteady Boundary Element Method

An unsteady boundary element method is employed to model and calculate the forces acting on three-dimensional self-propelled propulsors. The flow is assumed to be incompressible, irrotational, and inviscid, such that flow is governed by Laplace's equation as $\nabla^2\phi^* = 0$, where ϕ^* is the perturbation potential in a ground-fixed inertial frame of reference. There is a general solution to Laplace's equation subject to 1) a no-flux boundary condition on the surface of the propulsor, and 2) a far-field boundary condition that any perturbations to the flow should decay with a certain distance from the propulsor. The no-flux boundary condition is enforced with a Dirichlet boundary condition at each time step on the propulsor's surface. Then, the general solution of the Laplace's equation is reduced to find a distribution of doublet and source elements on the surface and the wake of the propulsor. The far-field boundary condition is fulfilled by the doublet and source elements' elementary solutions.

To solve the problem numerically, the wake and the propulsor are discretized into a constant number of quadrilateral boundary elements with a collocation point positioned at the element's center and moved just inside the body by 15% of the distance of the half-thickness of the body [21]. An explicit Kutta condition is imposed at the trailing edge where the vorticity is set to zero. During each time step, a wake doublet element from the previous time step is shed with a strength that satisfies Kelvin's condition. The wake deformation and rollup are achieved by letting the wake elements freely advect with the local velocity field by imposing the desingularized Biot–Savart Law introduced by Krasny [34]. The tangential perturbation velocity on the surface of the body is determined by a local differentiation of the perturbation velocity potential. Then, the unsteady Bernouilli equation is used to determine the pressure field acting on the propulsor body. Finally, the forces acting on the heaving and pitching propulsor are calculated by an integration of the pressure forces over its boundary. The self-propelled body dynamics is obtained through an equation of motion that permits only the streamwise translation of the propulsor. The body position and velocity, which are determined at the $(n+1)$th time step, are calculated through the trapezoidal rule and forward differencing scheme, as suggested by [3], respectively:

$$U_0^{n+1} = U_0^n + \frac{F_x^n}{m}\Delta t \tag{11}$$

$$x_b^{n+1} = x_b^n + \frac{1}{2}(U_0^{n+1} + U_0^n)\Delta t \tag{12}$$

where F_x^n and x_b correspond to the streamwise net force acting on the propulsor at the nth time step and the body position of the propulsor, respectively, and Δt refers to the time step. The details and validations of the numerical method can be found in [21] and the further applications and validations of the numerical solver can be found in [14,35,36].

B. Experimental Methods

Experimental data from three previously published studies [25,27,37] are used in the current study to validate the proposed scaling

laws. These previous studies used hydrofoils with NACA 0012 profiles, and prescribed sinusoidal motions described by Eqs. (2) and (3).

The first data set from [27,37] was for relatively high heave ratios from $0.82 \leq h^* \leq 1$. These studies were conducted in a towing tank and had a hydrofoil with a chord length of 0.07 m at a fixed chord-based Reynolds number of 2.1×10^4. Reference [37] reported data from an effectively two-dimensional foil with $\mathcal{R} = \infty$ and [27] reported data from a hydrofoil with $\mathcal{R} = 4.9$. The pitching axis of the hydrofoils in both studies is at the one-third-chord location. In these experiments the heave-to-chord ratio was fixed and equal to $h_0/c = 1$, the maximum pitching amplitude varied from 15 to 45 deg with an increment of 5 deg, and the frequency varied from 0.64 to 0.87 Hz to generate the Strouhal range of $0.3 \leq St \leq 0.5$.

The second data set from [25] had a fixed heave ratio of $h^* = 0$ throughout the study. The experiments were conducted in a recirculating water channel. The hydrofoils used in the study had a chord length of 0.1 m and a fixed chord-based Reynolds number of $Re = 3 \times 10^4$, for three aspect ratios of $\mathcal{R} = 1.0, 1.5$ and 2.0. The pitching frequency was varied from 0.5 to 2.0 Hz in increments of 0.25 Hz with the pitching axis located at the leading edge. The nondimensional peak-to-peak amplitude A^* varied from 0.2 to 0.5 in intervals of 0.1.

All the relevant input variables and parameters for the experimental studies are given in Table 1. More details of their methodologies can be found in [25,27,37].

IV. Extending Garrick's Linear Theory with Nonlinear Corrections

A. Garrick's Theory

Our scaling study starts with a full solution of small amplitude theory [19] for the thrust and power coefficients. In Garrick's solution [19], the thrust and power coefficients for a combined heaving and pitching motion are written as

$$C_T = c_1' \underbrace{\frac{4h_0^2}{A^2}[F^2+G^2]}_{\text{heave}} + c_2' \underbrace{\frac{4ch_0\theta_0}{A^2}\left[-(F^2+G^2)\left(\frac{1}{\pi k}\right)+\frac{G}{2}+\frac{F}{2\pi k}\right]}_{\text{heave+pitch}} + c_3' \underbrace{\frac{4c^2\theta_0^2}{A^2}\left\{(F^2+G^2)\left[\frac{1}{\pi^2k^2}+\left(\frac{1}{2}-a\right)^2\right]+\left(\frac{1}{4}-\frac{a}{2}\right)-\left(\frac{1}{2}-a\right)F-\frac{F}{\pi^2k^2}-\left(\frac{1}{2}+a\right)\frac{G}{\pi k}\right\}}_{\text{pitch}} \tag{13}$$

$$C_P = c_4' \underbrace{\frac{4h_0^2}{A^2}(F)}_{\text{heave}} + c_5' \underbrace{\frac{4ch_0\theta_0}{A^2}\left(\frac{F}{\pi k}-G\right)}_{\text{heave+pitch}} + c_6' \underbrace{\frac{4c^2\theta_0^2}{A^2}\left\{\frac{1}{2}\left(\frac{1}{2}-a\right)-\left(a+\frac{1}{2}\right)\left[F\left(\frac{1}{2}-a\right)+\frac{G}{\pi k}\right]\right\}}_{\text{pitch}} \tag{14}$$

In Eqs. (13) and (14), F and G are from Theodorsen's lift deficiency function and represent the real and imaginary parts of the function, respectively [18]. The thrust and power coefficients are separated into purely heaving, combined heaving and pitching, and purely pitching terms, as indicated by the underbraces. The model coefficients have values from Garrick's theory of $c_1' = c_2' = c_4' = c_5' = \pi^3/2$ and $c_3' = c_6' = \pi^3/8$. Garrick's theory assumes small amplitude motion and that the wake is nondeforming and planar. In this study, the simulations and experiments vary from small to large amplitude motions and the wakes are deforming and not planar. Ergo, the exact theoretical coefficients defined by Garrick are relaxed and left to be determined to obtain scaling relations that accurately reflect the current data sets. Now, with the relaxed coefficients, Eqs. (13) and (14) can be written with $4h_0^2/A^2 = h_0^{*2}$, $4ch_0\theta_0/A^2 = h_0^*\theta_0^*$, and $4c^2\theta_0^2/A^2 = \theta_0^{*2}$ being substituted in a more compact form:

$$C_T = c_1'' h_0^{*2} w_1(k) + c_2'' h_0^* \theta_0^* w_2(k) + c_3'' \theta_0^{*2} w_3(a,k) \tag{15}$$

$$C_P = c_4'' h_0^{*2} w_4(k) + c_5'' h_0^* \theta_0^* w_5(k) + c_6'' \theta_0^{*2} w_6(a,k) \tag{16}$$

B. Two-Dimensional Scaling Laws

To consider the scaling of performance for combined heaving and pitching two-dimensional propulsors, Garrick's combined heaving and pitching linear theory is extended with nonlinear corrections similar to those proposed by [22] for pitching two-dimensional propulsors. Garrick's linear theory is modified by three nonlinear corrections: a form drag term, a large-amplitude separating shear layer term, and a vortex proximity term, however, the latter two corrections have been modified from those presented in [22] to account for combined heaving and pitching motions, whereas the form drag term remains solely dependent upon the pitching portion of the motion. Now, the new scaling law for the thrust coefficient is

$$C_T = c_1 \underbrace{(1/4 - a/2)\theta_0^{*2}}_{\zeta_1} + c_2 \underbrace{h_0^{*2} w_1(k)}_{\zeta_2} + c_3 \underbrace{h_0^* \theta_0^* w_2(k)}_{\zeta_3} + c_4 \underbrace{\theta_0^{*2} w_3'(a,k)}_{\zeta_4} + c_5 \underbrace{A_p^*}_{\zeta_5} \tag{17}$$

$$\text{where: } w_3'(a,k) = \left\{(F^2+G^2)\left[\frac{1}{\pi^2k^2}+\left(\frac{1}{2}-a\right)^2\right]-\left(\frac{1}{2}-a\right)F - \frac{F}{\pi^2k^2}-\left(\frac{1}{2}+a\right)\frac{G}{\pi k}\right\}$$

$$A_p^* = 2\sin(\theta_0)$$

Equation (17) presents the thrust coefficient that is a combination of the added mass force from pitching ($c_1\zeta_1$), and the circulatory forces from heave ($c_2\zeta_2$), combined heave and pitch ($c_3\zeta_3$), and pitch ($c_4\zeta_4$), as well as a form drag term ($c_5\zeta_5$) that comes from the pitch portion of the motion only because it is physically due to the projected frontal area of the propulsor. Note that the added mass portion of the force from pitching motions has been separated from the circulatory force for pitching motions, thus necessitating the use of the prime on $w_3'(a,k)$.

The new scaling law for the power consumption is

$$C_P = c_6 \underbrace{(1/4 - a/2)\theta_0^{*2}}_{\zeta_6} + c_7 \underbrace{h_0^{*2} w_4(k)}_{\zeta_7} + c_8 \underbrace{h_0^* \theta_0^* w_5(k)}_{\zeta_8} + c_9\zeta_9 + c_{10}\zeta_{10} \tag{18}$$

$$\text{where } \zeta_9 = \left(\frac{k^*}{k^*+1}\right) St_p \theta_0 g_9(h_0^*, \theta_0^*, \theta_0, a),$$

$$\zeta_{10} = St^2 k^* g_{10}(h_0^*, \theta_0^*, \theta_0, a) \tag{18}$$

and,

$$g_9(h_0^*, \theta_0^*, \theta_0, a) = h_0^{*2} + h_0^*\theta_0^*\left(\frac{3}{4}-a\right)\cos(\theta_0) + \theta_0^{*2}\left[\frac{1}{4}\left(\frac{1}{2}-a\right)(1-a)\right]\cos^2(\theta_0)$$

$$g_{10}(h_0^*, \theta_0^*, \theta_0, a) = h_0^{*3} + h_0^{*2}\theta_0^*\left[\frac{1}{2}\left(\frac{1}{2}-a\right)(1-a)\right]\cos(\theta_0) + \ldots$$
$$h_0^*\theta_0^{*2}\left[\frac{1}{4}\left(2\left(\frac{1}{2}-a\right)(1-a) + \left(\frac{1}{2}-a\right)^2\right)\right]\cos^2(\theta_0) + \ldots$$
$$\theta^{*3}\left[\frac{1}{8}\left(\frac{1}{2}-a\right)^2(1-a)\right]\cos^3(\theta_0)$$

Here, St_p and k^* represent the Strouhal number based on the pitching amplitude and a modified reduced frequency, respectively. They are defined as $St_p = (fA_p)/U$ and $k^* = k/(1+4St^2)$. Similar to the thrust coefficient, the power coefficient is a combination of the added-mass power from pitching ($c_6\zeta_6$), the circulatory power from heave ($c_7\zeta_7$), the circulatory power from combined heave and pitch ($c_8\zeta_8$), as well as the circulatory nonlinear correction terms modeling the power due to a large-amplitude separating shear layer ($c_9\zeta_9$) and due to the proximity of the trailing-edge vortex ($c_{10}\zeta_{10}$). In contrast to the thrust coefficient, in Eq. (18), the pitch-only circulatory term was neglected without much penalty to the data collapse (see Sec. V). The large-amplitude separating shear layer and vortex proximity power corrections introduced in [22] have also been modified to account for changes that come with heaving motions (see Appendix for details). All of the terms in the scaling relations are first developed for the lift and are then propagated into thrust and power.

C. Three-Dimensional Scaling Laws

To account for three-dimensional effects of the propulsors, the two-dimensional scaling laws presented earlier will be modified. First, we will consider the power scaling law. Previously for pure pitching motions, it was identified [25] that an elliptical vortex ring correction for the separating shear layer term ($c_9\,\zeta_9$), and the vortex proximity term ($c_{10}\,\zeta_{10}$) was necessary. Now, modifying that correction for heaving motions results in new scaling terms ζ_9' and ζ_{10}' as

$$\zeta_9' = \left(\frac{\gamma k^*}{\gamma k^* + 1}\right) St_p\theta_0\, g_9(h_0^*, \theta_0^*, \theta_0, a)$$
$$\text{and} \quad \zeta_{10}' = \gamma St^2 k^*\, g_{10}(h_0^*, \theta_0^*, \theta_0, a)$$
$$\text{with:} \quad \gamma = \frac{1}{2}\left[E(m_2) + \frac{E(m_1)}{\mathcal{AR}\sqrt{4kk^*}}\right]$$

Here, m_1 and m_2 are elliptic moduli where $m_1 = \sqrt{1-4\mathcal{AR}kk^*}$ and $m_2 = \sqrt{1+4\mathcal{AR}kk^*}$ and E corresponds to the complete elliptic integral of the second kind [25]. For more details on the development of these modifications, see Appendix B in [25].

Additionally, the two-dimensional scaling model will be corrected by applying classic aerodynamic and hydrodynamic theory corrections to the circulatory [38] and noncirculatory [39] terms as follows:

$$C_T = c_1\,\zeta_1\left(\frac{\mathcal{AR}}{\mathcal{AR}+1}\right) + (c_2\,\zeta_2 + c_3\,\zeta_3 + c_4\,\zeta_4)\left(\frac{\mathcal{AR}}{\mathcal{AR}+2}\right) + c_5\,\zeta_5,$$

$$C_P = c_6\,\zeta_1\left(\frac{\mathcal{AR}}{\mathcal{AR}+1}\right) + \left(c_7\,\zeta_7 + c_8\,\zeta_8 + c_9\,\zeta_9' + c_{10}\,\zeta_{10}'\right)\left(\frac{\mathcal{AR}}{\mathcal{AR}+2}\right)$$

Dividing by the added mass correction, $\mathcal{AR}/(\mathcal{AR}+1)$ leads to the following:

$$C_T\left(\frac{\mathcal{AR}+1}{\mathcal{AR}}\right) = c_1\,\zeta_1 + (c_2\,\zeta_2 + c_3\,\zeta_3 + c_4\,\zeta_4)\left(\frac{\mathcal{AR}+1}{\mathcal{AR}+2}\right) + c_5\,\zeta_5\left(\frac{\mathcal{AR}+1}{\mathcal{AR}}\right)$$

$$C_P\left(\frac{\mathcal{AR}+1}{\mathcal{AR}}\right) = c_6\,\zeta_1 + \left(c_7\,\zeta_7 + c_8\,\zeta_8 + c_9\,\zeta_9' + c_{10}\,\zeta_{10}'\right)\left(\frac{\mathcal{AR}+1}{\mathcal{AR}+2}\right)$$

Finally, this modification creates a compact three-dimensional form of scaling relations as

$$C_T^* = c_1\zeta_1 + c_2\zeta_2^* + c_3\zeta_3^* + c_4\zeta_4^* + c_5\zeta_5^* \tag{19}$$

$$C_P^* = c_6\zeta_6 + c_7\zeta_7^* + c_8\zeta_8^* + c_9\zeta_9^* + c_{10}\zeta_{10}^* \tag{20}$$

In the thrust coefficient equation $C_T^* = C_T\,[(\mathcal{AR}+1)/\mathcal{AR}]$, and the various ζ^* are defined as $\zeta_{2,3,4}^* = \zeta_{2,3,4}[(\mathcal{AR}+1)/(\mathcal{AR}+2)]$ and $\zeta_5^* = \zeta_5[(\mathcal{AR}+1)/\mathcal{AR}]$. In the power coefficient equation $C_P^* = C_P\,[(\mathcal{AR}+1)/\mathcal{AR}]$, and the various ζ^* are defined as $\zeta_{7,8}^* = \zeta_{7,8}[(\mathcal{AR}+1)/(\mathcal{AR}+2)]$ and $\zeta_{9,10}^* = \zeta_{9,10}'[(\mathcal{AR}+1)/(\mathcal{AR}+2)]$.

By following the same transformation introduced in Sec. II.C, the final scaling relations normalized by dynamic pressure may also be written as

$$C_T^{\text{dyn}^*} = (c_1\zeta_1 + c_2\zeta_2^* + c_3\zeta_3^* + c_4\zeta_4^* + c_5\zeta_5^*)2St^2 \tag{21}$$

$$C_P^{\text{dyn}^*} = (c_6\zeta_6 + c_7\zeta_7^* + c_8\zeta_8^* + c_9\zeta_9^* + c_{10}\zeta_{10}^*)2St^2 \tag{22}$$

V. Results and Discussion

The numerical input parameters (Table 1) form more than 500 three-dimensional and self-propelled simulations. In the simulations, the reduced frequency and Strouhal number vary in the ranges of $0.04 < k < 1.32$ and $0.07 < St < 0.31$, respectively.

Figure 2 presents the thrust and power coefficients, calculated as in Eq. (9), as functions of aspect ratio, Li number, and the reduced frequency for all motion amplitudes considered here. From black to white the marker colors correspond to dimensionless amplitude or aspect ratio changing from low to high values, whereas the marker styles represent different Li. The thrust and power of a heaving and pitching hydrofoil vary widely with its input parameters. Because the simulations are self-propelled, then high-amplitude motions produce high swimming speeds, in general, leading to lower reduced frequencies, as seen in Figs. 2a and 2b. When all variables are fixed and the Li number increases there is a subsequent reduction in the swimming speed that leads to an increase in the reduced frequency, although this trend is difficult to decipher from Fig. 2 because many variables are changing in these data. Figures 2c and 2d show that in general as the aspect ratio increases, so too does the thrust and power. Figure 3 shows an excellent collapse of the numerical data (presented in Fig. 2), when plotted as a function of three-dimensional scaling relations proposed in Eqs. (19) and (20). The collapsed data follow a line of slope 1 for both the thrust coefficient and power coefficient within ±12% (thrust) and ±10% (power) of the predicted scaling law. The values of the constants are obtained by minimizing the squared residuals between the data and the scaling law prediction. The constants in the thrust law are $c_1 = 2.69$, $c_2 = 18.37$, $c_3 = 3.39$, $c_4 = 19.85$, and $c_5 = -0.16$, whereas for the power law they are $c_6 = 5.03$, $c_7 = 19.29$, $c_8 = 10.05$, $c_9 = 11.61$, and $c_{10} = 13.44$.

To validate that the scaling laws equally apply to viscous flows, the compilation of experimental data is plotted vs the scaling law predictions in Fig. 4. The experimental data have a reduced frequency range of $0.15 < k < 1.34$ and a Strouhal number range of $0.06 \leq St < 0.45$. The marker colors represents different aspect ratios. The circle and triangle marker types indicate $Re = 21{,}000$ and $Re = 30{,}000$, respectively. The dashed lines on the thrust and power

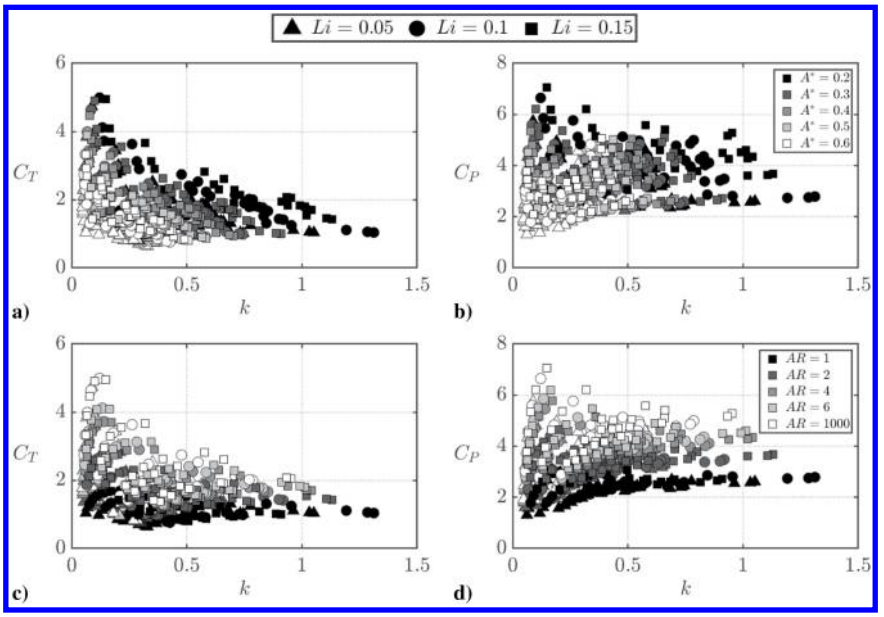

Fig. 2 The (a, c) thrust and (b, d) power coefficient data from the self-propelled simulations as a function of reduced frequency.

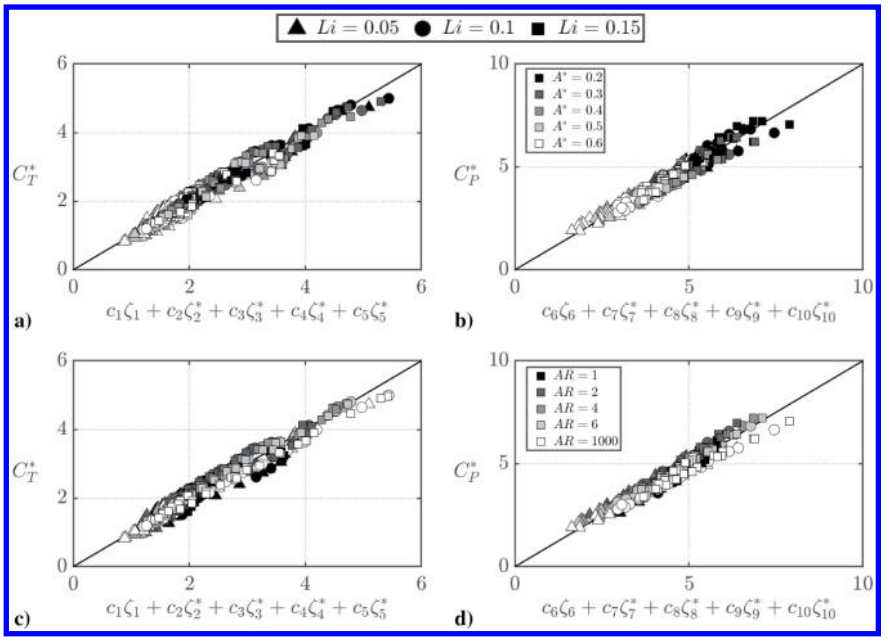

Fig. 3 Scaling of the (a, c) thrust and (b, d) power coefficient data for all motion amplitudes and aspect ratios considered in the simulations.

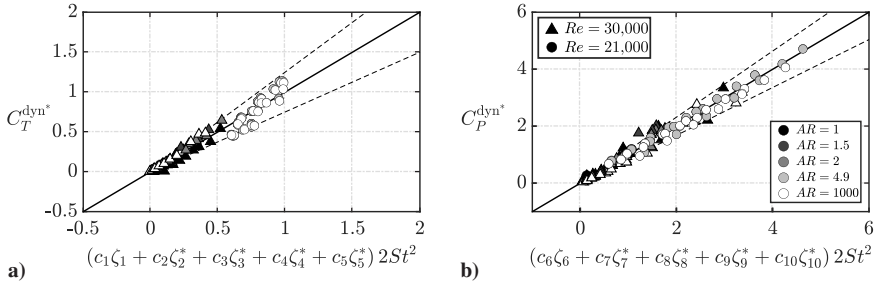

Fig. 4 Scaling of the a) thrust and b) power coefficient data for all motion amplitudes and aspect ratios considered in the experiments (viscous flow cases).

graphs represent ±25% and ±16% error, respectively. For both thrust and power, we see a collapse of the data nearly within these limits. The experimentally determined constants for the thrust equation are $c_1 = 3.14$, $c_2 = 7.68$, $c_3 = 8.62$, $c_4 = -20.05$, and $c_5 = -0.79$, and for the power equation they are $c_6 = 7.37$, $c_7 = 24.89$, $c_8 = 18.66$, $c_9 = -369.41$, and $c_{10} = 206.85$.

Our scaling relations show a good collapse of the data for a wide range of Reynolds numbers from $Re = 21{,}000$ and $Re = 30{,}000$ in the experiments to $Re = \infty$ in the inviscid simulations. Although, it should be noted that the determined coefficients are different between the simulations and the experiments. For example, the c_9 coefficient alters its sign when it is fitted to the experimental data, indicating

power extraction instead of power consumption like the other coefficients. This is happening most likely because of a viscosity-related phase shift between the velocity of the propulsor and the lift term scaled by c_9. In the numerics, this phase shift is not captured because the simulations are inviscid. As expected based on physical grounds, in both simulations and experiments no sign changes are seen in the added mass power and thrust terms.

To approach universal constants it would be important to account for the Reynolds number variation in the thrust and power data, as pioneered by [40]. However, the common agreement in the basic scaling terms for inviscid and viscous flows indicates that the dominant flow physics are inviscid in nature. The small differences between the scaling law agreement in the experiments and the simulations may be attributed to secondary viscous effects, such as the known Reynolds number dependency of all of the coefficients [40].

The data collapsed to a line of slope 1 for both numerical and experimental cases verifies that the dominant flow physics of three-dimensional heaving and pitching propulsors across a broad range of St, A^*, h^*, and $\mathcal{AR}$ is captured by the newly developed scaling laws.

VI. Sensitivity of the Scaling Laws

A sensitivity analysis is performed to more deeply understand which modifications of Garrick's theory are most important for modeling the predominant physics of three-dimensional combined heaving and pitching hydrofoils. Figure 5 shows the sensitivity of the experimental data collapse to the scaling laws with and without the nonlinear terms and modified coefficients. Figures 5a and 5b present the collapse of the experimental data with the full scaling model of the thrust ($R^2 = 0.9416$) and power coefficients ($R^2 = 0.9810$) as shown in Fig. 4. Figures 5c and 5d show the scaling relations without the contribution of the nonlinear terms in the thrust ($c_5\zeta_5^*$) and power ($c_9\zeta_9^*$, $c_{10}\zeta_{10}^*$) relations. Without the nonlinear terms, the scaling relations correspond to the modified Garrick model with empirically determined coefficients and three-dimensional corrections. Now, it's clear that the nonlinear form drag term added to the thrust plays no significant role in improving the accuracy of the modified Garrick model (thrust relation without the nonlinear term: $R^2 = 0.9405$). This is not surprising because it has been previously determined to be a mild correction for purely pitching motions [22]. The nonlinear power corrections are seen to significantly improve the modified Garrick model (power relation without nonlinear terms: $R^2 = 0.9565$). Without the nonlinear power terms, the data is still stratified based on the aspect ratio even with the three-dimensional corrections. Moreover, with the nonlinear power terms included, the $Re = 30{,}000$ data is observed to fall more in line with the scaling trend line, whereas the $Re = 21{,}000$ data is observed to collapse more tightly around the trend line. Figures 5e and 5f show the modified Garrick model when the coefficients are *not* empirically determined, that is, they are set to their theoretical values. If the theoretically derived coefficients are used, the scaling relations poorly model the performance (thrust relation: $R^2 = 0.9057$; power relation: $R^2 = 0.2546$), with the thrust and power being over- and underpredicted, respectively.

Figures 6a and 6b again present the experimental data collapse for the full scaling model. Figures 6c and 6d show the collapse of the data when the added mass terms are neglected in the scaling laws (thrust: $R^2 = 0.8022$; power: $R^2 = 0.8712$), whereas Figs. 6e and 6f show the collapse when the circulatory terms are neglected from the full model (thrust: $R^2 = 0.1243$; power: $R^2 = -1.324$). Given the wide range of h^* for the data, neither the added mass nor the circulatory terms can be neglected and still produce an accurate scaling model. However, within a more limited range of h^* this is possible. For example, for high h^*, modeling only the circulatory forces does produce an accurate model of the thrust and power [26], although, without modeling the added mass forces, some subtle trends in the efficiency are missed.

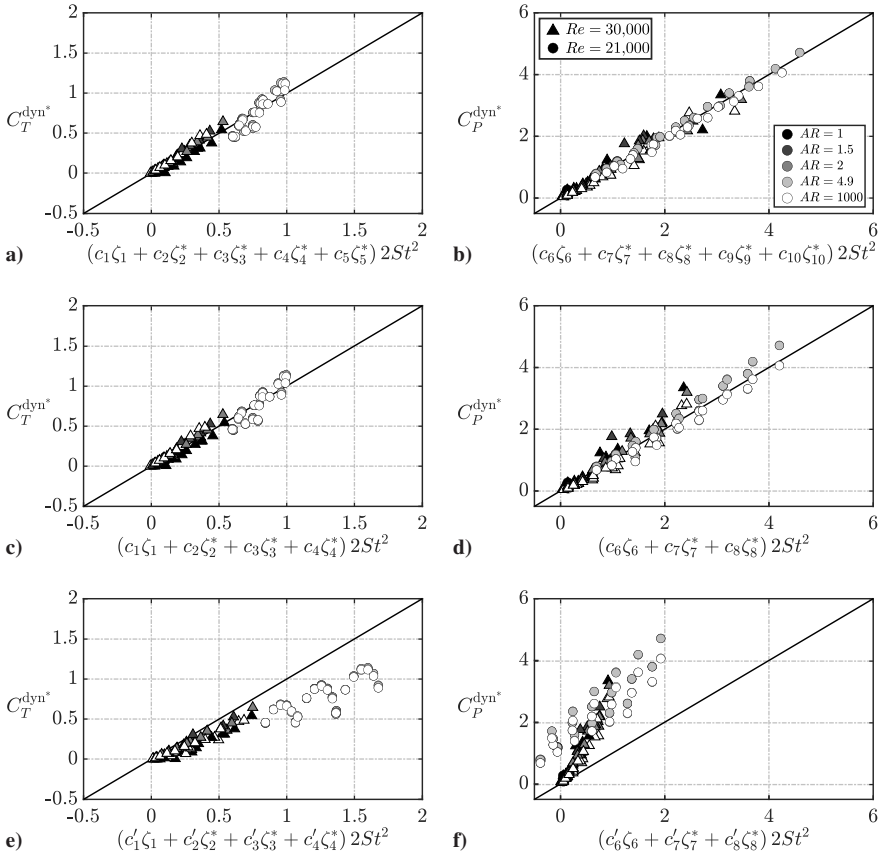

Fig. 5 Sensitivity of the scaling laws to the nonlinear terms and modified coefficients using experimental data. Full scaling model for the a) thrust and b) power coefficients. Modified Garrick model with empirically determined coefficients and three-dimensional corrections for the c) thrust and d) power coefficients. Modified Garrick model with theoretically derived coefficients and three-dimensional corrections for the e) thrust and f) power coefficients.

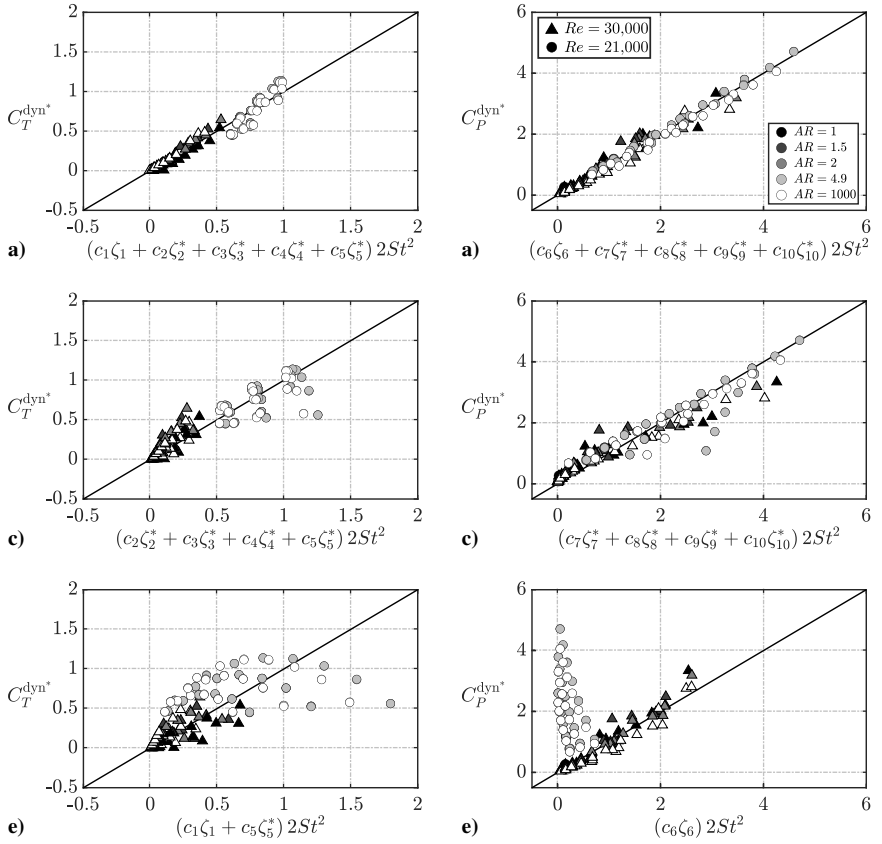

Fig. 6 Sensitivity of the scaling laws to the added mass and circulatory terms using experimental data. Full scaling model for the a) thrust and b) power coefficients. Full scaling model *neglecting* the added mass terms for the c) thrust and d) power coefficients. Full scaling model *neglecting* the circulatory terms for the e) thrust and f) power coefficients.

VII. Derived Physical Insight

Next, we use the developed scaling relations as a tool to understand the effects of kinematics and aspect ratio on the propulsor efficiency. The scaling law for efficiency is simply the ratio of the scaling laws developed for the thrust and power coefficients, which becomes

$$\eta = \frac{c_1\,\zeta_1 + (c_2\,\zeta_2 + c_3\,\zeta_3 + c_4\,\zeta_4)\,[(\mathcal{R}+1)/(\mathcal{R}+2)] + c_5\,\zeta_5\,[(\mathcal{R}+1)/(\mathcal{R})]}{c_6\,\zeta_6 + (c_7\,\zeta_7 + c_8\,\zeta_8 + c_9\,\zeta_9' + c_{10}\,\zeta_{10}')\,[(\mathcal{R}+1)/(\mathcal{R}+2)]} \tag{23}$$

The experimentally determined coefficients are used in this section for analyzing the efficiency scaling law (see Sec. V for the coefficient values).

Next, the scaling relations are used to investigate the efficiency trends when h^*, A^*, $\mathcal{R}$, Li, and a are changed independently. As a reference case, $\mathcal{R} = 3$, $A^* = 1$, and $Li = 0.2$ are chosen because they correspond to typical values for bio-inspired locomotion. Figure 7 shows the efficiency plotted against h^* when the pitch axis is located at the leading edge ($a = -1$). In Fig. 7a the lines represent various $\mathcal{R}$ with $A^* = 1$ and $Li = 0.2$. In Fig. 7b the lines represent various A^* with $\mathcal{R} = 3$ and $Li = 0.2$. In Fig. 7c the lines represent various Li with $A^* = 1$ and $\mathcal{R} = 3$. The line colors are mapped to the variations of $\mathcal{R}$, A^*, and Li from small (black) to large (white) values.

In all figures, it can be seen that efficiency is maximized when h^* reaches an optimal value. Figure 7a shows that as the aspect ratio increases the optimal h^* decreases, and that for pitch-dominated motions the efficiency is relatively insensitive to changes in aspect ratio. In Fig. 7b, high efficiency occurs for large dimensionless amplitudes A^*. This observation is consistent with the argument put forth by [41], in which they proposed that large-amplitude motions are more efficient than small-amplitude motions. Reference [41] also stated that optimal efficiency should occur when $h^* = 0.5$, where heaving and pitching motions contribute equally to the total motion. However, this assertion is based on a highly simplified model where minimizing the power consumption, which

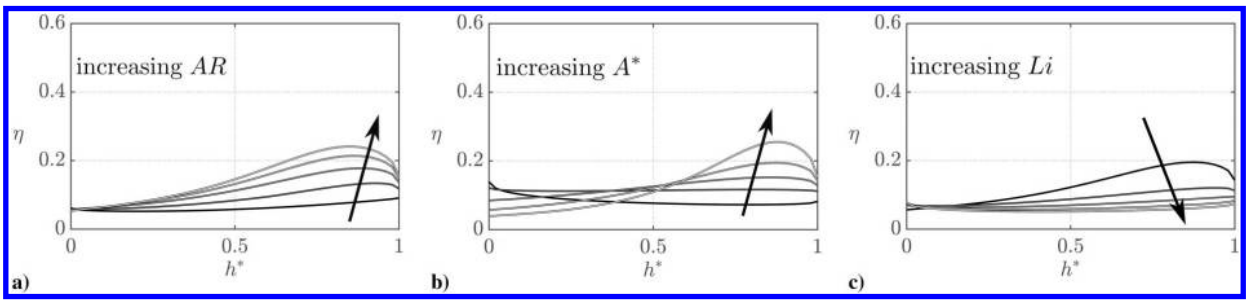

Fig. 7 Efficiency plotted against h^* for a) $A^* = 1$, $1 \le \mathcal{R} \le 5$, and $Li = 0.2$, b) $\mathcal{R} = 3$, $0.2 \le A^* \le 1.5$, and $Li = 0.2$, and c) $A^* = 1$, $\mathcal{R} = 3$, and $0.2 \le Li \le 1$ when pitching axis at leading edge ($a = -1$).

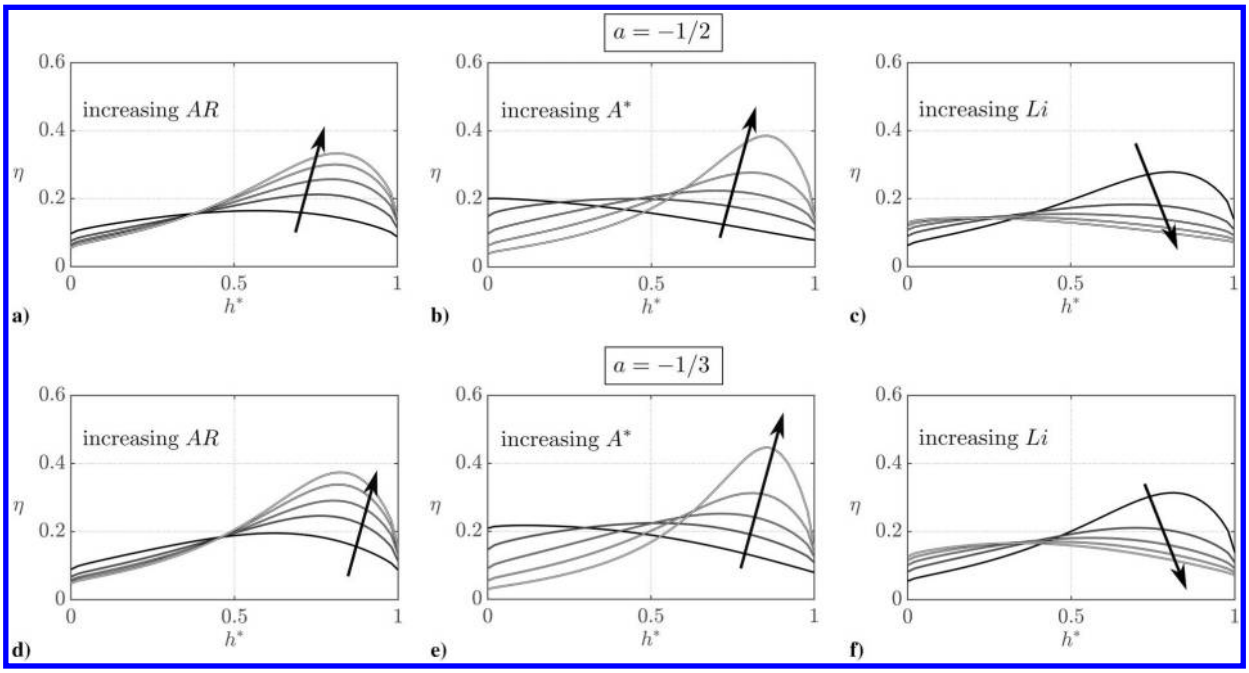

Fig. 8 Efficiency plotted against h^* for (a, d) $A^* = 1, 1 \leq \mathcal{AR} \leq 5$, and $Li = 0.2$, (b, e) $\mathcal{AR} = 3, 0.2 \leq A^* \leq 1.5$, and $Li = 0.2$, and (c, f) $A^* = 1, \mathcal{AR} = 3$, and $0.2 \leq Li \leq 1$ when pitching axis at one-third chord ($a = -1/3$) and at midchord ($a = 0$).

occurs at $h^* = 0.5$, will lead to the maximum efficiency. In fact, it is routinely shown that unsteady foils may have different conditions that minimize their power consumption from those that maximize their efficiency [42–44], and that peak efficiencies for *large-amplitude* ($A^* > 1$) combined heaving and pitching motions occur for $h^* > 0.7$ [26,44]. Indeed, Fig. 7b shows that the optimal value is not near $h^* = 0.5$ in this data, but is, in fact, closer to $h^* = 0.8$ for the most efficient cases. When $A^* < 1$, peak efficiencies occur for pitch-dominated motions ($h^* < 0.5$) and for $A^* \geq 1$ they occur for heave-dominated motions ($h^* > 0.5$). In fact, for cases close to pure pitching where $h^* < 0.25$, the efficiency increases when A^* decreases, whereas that trend begins to reverse for $h^* > 0.25$. It is also observed that increasing the Li number decreases the propulsive efficiency for $h^* > 0.1$, however, there is a reversal of this trend for $h^* < 0.1$ (this trend can be more clearly observed in Fig. 8). This behavior is a consequence of several concurrent effects. For example, an increase in Li leads to an increase in drag on the body, a decrease in swimming speed, and, subsequently, an increase in reduced frequency. An increase in reduced frequency results in a decrease in the efficiency for heave-dominated motions [13,14,19,22,45] and vice versa for pitch-dominated motions. These distinctly different regimes are due to pitch-dominated motions being driven by added mass forces, whereas heave-dominated motions are driven by circulatory forces [36,44]. The main conclusion from Fig. 7 is that the highest efficiencies occur for a narrow range of h^* from $0.75 < h^* < 0.94$ for $A^* \geq 1$.

Figure 8 shows the efficiency variation as functions of h^*, $\mathcal{AR}$, A^*, and Li for different pitch axis locations. Figures 8(a, d), (b, e), and (c, f) indicate the same trends as Figs. 7a–7c, respectively. Now, it is observed that the variation in the pitching axis changes the maximum efficiency peak and optimum h^* value. When the pitch axis moves from the leading edge toward the midchord, the maximum efficiency increases for all the parameter variations considered here.

VIII. Conclusions

New three-dimensional scaling relations are developed for the power consumption and thrust generation of combined heaving and pitching propulsors by extending the three-dimensional pitching scaling laws introduced by [25] to consider combined heaving and pitching motions. The developed scaling laws are shown to predict inviscid numerical data and experimental data well, within ±25% and ±16% of the thrust and power data, respectively. The scaling laws reveal that both the circulatory and added mass forces are important when considering a wide range of motion amplitudes, and that nonlinear corrections to classic linear theory are essential to modeling the power performance across this wide aspect ratio range. By using the scaling laws as a tool, it is obtained that peak efficiencies occur when $A^* > 1$ and for these large amplitude motions there is an optimal h^* that maximizes the efficiency in the narrow range of $0.75 < h^* < 0.94$. Finally, the scaling laws show that to further improve efficiency in this high-efficiency regime, the aspect ratio and dimensionless amplitude should be increased, whereas the Lighthill number should be decreased (lower drag and/or a larger propulsor planform area to wetted surface area ratio), and the pitch axis should be located downstream of the leading edge.

Appendix: Derivation of Scaling Relations

Two nonlinear lift terms are introduced in [22]: the lift due to the separating shear layer L_{sep} and the proximity of the trailing-edge vortex L_{prox}. These terms are determined based on the balance between the cross-stream velocity originated at the trailing edge due to the trailing-edge vortex shedding and the same component of the velocity induced by the bound vortex Γ_b. The balance between the components ensures the Kutta condition at the trailing edge and formulates a relation for the additional bound circulation as $\Gamma_b = \Gamma_0 - \Gamma_1$. In here, Γ_0 corresponds to the quasi-steady bound circulation that arises from the motion of the propulsor alone without the presence of the wake. In opposition, the additional bound circulation Γ_1 arises only from the influence of the wake.

These terms are modified to fully account for combined heaving and pitching motion in the current study. We started with the separating shear layer term,

$$L_{\text{sep}} = \rho s(\Gamma_0 + \Gamma_1)\frac{dx}{dt} \quad \text{where: } \frac{dx}{dt} = c\dot{\theta}\sin\theta \tag{A1}$$

The dot over some terms corresponds to the time rate of change. When we take the time-average the Γ_0 term goes to zero due to near-orthogonality between $\dot{\theta}$ and $\sin\theta$. Then,

$$P_{\text{sep}} = \rho s\Gamma_1 c\dot{\theta}\sin\theta\left[\dot{h} + 1/2(1-a)c\dot{\theta}\cos(\theta)\right] \tag{A2}$$

where Γ_1 is the additional circulation determined by [22] as

$$\Gamma_1 \propto -\Gamma_0\left(\frac{k^*}{k^*+1}\right) \tag{A3}$$

For large-amplitude, combined heaving and pitching motions, the bound circulation is defined as

$$\Gamma_0 \propto -c\left[\dot{h} + c\dot{\theta}\cos(\theta)\frac{1}{2}\left(\frac{1}{2}-a\right)\right] \tag{A4}$$

with a corresponding to pitch axis location as defined by [19].

Now, substituting the relation (A4) into (A2), the following power relation for the separating shear layer term can be obtained:

$$P_{\text{sep}} = \rho S_p c f^3 \theta_0 \sin\theta_0\left(\frac{k^*}{k^*+1}\right)\left[\dot{h} + 1/2(1-a)c\dot{\theta}\cos(\theta)\right] \times\left[\dot{h} + c\dot{\theta}\cos(\theta)\frac{1}{2}\left(\frac{1}{2}-a\right)\right] \tag{A5}$$

The second explicitly nonlinear correction to the power is due to the proximity of the trailing-edge vortex, where the lift from this term is

$$L_{\text{prox}} = \rho s(\Gamma_0 + \Gamma_1)u_{\text{ind}} \tag{A6}$$

Here, u_{ind} is the velocity induced at the trailing edge by the trailing-edge vortex. Derivations can be found in [22] for two-dimensional pitching foils and [25] for three-dimensional pitching foils. Because Γ_1 is a perturbation of Γ_0, we neglect Γ_1. Then,

$$L_{\text{prox}} = \rho s\Gamma_0 u_{\text{ind}} \quad \text{where: } u_{\text{ind}} = \frac{\Gamma_0 fSt}{U(1+4St^2)} \tag{A7}$$

Consequently, the power scaling from the proximity of the trailing-edge vortex is obtained as

$$P_{\text{prox}} = \frac{\rho S_p c f^4 St}{U(1+4St^2)}\left[\dot{h} + 1/2(1-a)c\dot{\theta}\cos(\theta)\right] \times\left[\dot{h} + c\dot{\theta}\cos(\theta)\frac{1}{2}\left(\frac{1}{2}-a\right)\right]^2 \tag{A8}$$

Acknowledgments

This work was funded by the Office of Naval Research (ONR) under the Multidisciplinary University Research Initiative (MURI) program (grant no. N00014-14-1-0533).

References

[1] Buchholz, J. H. J., and Smits, A. J., "The Wake Structure and Thrust Performance of a Rigid Low-Aspect-Ratio Pitching Panel," *Journal of Fluid Mechanics*, Vol. 603, May 2008, pp. 331–365. https://doi.org/10.1017/S0022112008000906

[2] Borazjani, I., and Sotiropoulos, F., "Numerical Investigation of the Hydrodynamics of Carangiform Swimming in the Transitional and Inertial Flow Regimes," *Journal of Experimental Biology*, Vol. 211, No. 10, 2008, pp. 1541–1558. https://doi.org/10.1242/jeb.015644

[3] Borazjani, I., and Sotiropoulos, F., "Numerical Investigation of the Hydrodynamics of Anguilliform Swimming in the Transitional and Inertial Flow Regimes," *Journal of Experimental Biology*, Vol. 212, No. 4, 2009, pp. 576–592. https://doi.org/10.1242/jeb.025007

[4] Masoud, H., and Alexeev, A., "Resonance of Flexible Flapping Wings at Low Reynolds Number," *Physical Review E*, Vol. 81, No. 5, 2010, Paper 056304. https://doi.org/10.1103/PhysRevE.81.056304

[5] Dewey, P. A., Carriou, A., and Smits, A. J., "On the Relationship Between Efficiency and Wake Structure of a Batoid-Inspired Oscillating Fin," *Journal of Fluid Mechanics*, Vol. 691, Jan. 2012, pp. 245–266. https://doi.org/10.1017/jfm.2011.472

[6] Moored, K. W., Dewey, P. A., Boschitsch, B. M., Smits, A. J., and Haj-Hariri, H., "Linear Instability Mechanisms Leading to Optimally Efficient Locomotion with Flexible Propulsors," *Physics of Fluids*, Vol. 26, No. 4, 2014, Paper 041905. https://doi.org/10.1063/1.4872221

[7] Moored, K. W., Dewey, P. A., Smits, A. J., and Haj-Hariri, H., "Hydrodynamic Wake Resonance as an Underlying Principle of Efficient Unsteady Propulsion," *Journal of Fluid Mechanics*, Vol. 708, Oct. 2012, pp. 329–348. https://doi.org/10.1017/jfm.2012.313

[8] Mackowski, A. W., and Williamson, C. H. K., "Direct Measurement of Thrust and Efficiency of an Airfoil Undergoing Pure Pitching," *Journal of Fluid Mechanics*, Vol. 765, Feb. 2015, pp. 524–543. https://doi.org/10.1017/jfm.2014.748

[9] King, J. T., Kumar, R., and Green, M. A., "Experimental Observations of the Three-Dimensional Wake Structures and Dynamics Generated by a Rigid, Bioinspired Pitching Panel," *Physical Review Fluids*, Vol. 3, No. 3, 2018, Paper 034701. https://doi.org/10.1103/PhysRevFluids.3.034701

[10] Brooks, S. A., and Green, M. A., "Experimental Study of Body-Fin Interaction and Vortex Dynamics Generated by a Two Degree-of-Freedom Fish Model," *Biomimetics*, Vol. 4, No. 67, 2019, pp. 1–23. https://doi.org/10.3390/biomimetics4040067

[11] Green, M. A., Rowley, C. W., and Smits, A. J., "The Unsteady Three-Dimensional Wake Produced by a Trapezoidal Pitching Panel," *Journal of Fluid Mechanics*, Vol. 685, Oct. 2011, pp. 117–145. https://doi.org/10.1017/jfm.2011.286

[12] Kang, C. K., Aono, H., Cesnik, C. E. S., and Shyy, W., "Effects of Flexibility on the Aerodynamic Performance of Flapping Wings," *Journal of Fluid Mechanics*, Vol. 689, Dec. 2011, pp. 32–74. https://doi.org/10.1017/jfm.2011.428

[13] Dewey, P. A., Boschitsch, B. M., Moored, K. W., Stone, H. A., and Smits, A. J., "Scaling Laws for the Thrust Production of Flexible Pitching Panels," *Journal of Fluid Mechanics*, Vol. 732, Oct. 2013, pp. 29–46. https://doi.org/10.1017/jfm.2013.384

[14] Quinn, D. B., Moored, K. W., Dewey, P. A., and Smits, A. J., "Unsteady Propulsion Near a Solid Boundary," *Journal of Fluid Mechanics*, Vol. 742, March 2014, pp. 152–170. https://doi.org/10.1017/jfm.2013.659

[15] Quinn, D. B., Lauder, G. V., and Smits, A. J., "Scaling the Propulsive Performance of Heaving Flexible Panels," *Journal of Fluid Mechanics*, Vol. 738, Jan. 2014, pp. 250–267. https://doi.org/10.1017/jfm.2013.597

[16] Das, A., Shukla, R. K., and Govardhan, R. N., "Existence of a Sharp Transition in the Peak Propulsive Efficiency of a Low-*Re* Pitching Foil," *Journal of Fluid Mechanics*, Vol. 800, Aug. 2016, pp. 307–326. https://doi.org/10.1017/jfm.2016.399

[17] Bainbridge, R., "The Speed of Swimming of Fish as Related to Size and to the Frequency and Amplitude of the Tail Beat," *Journal of Experimental Biology*, Vol. 35, No. 1, 1958, pp. 109–133. https://doi.org/10.1242/jeb.35.1.109

[18] Theodorsen, T., "General Theory of Aerodynamic Instability and the Mechanism of Flutter," NACA TR 496, 1935, pp. 413–433.

[19] Garrick, I. E., "Propulsion of a Flapping and Oscillating Airfoil," NACA TR 567, 1936, pp. 419–427.

[20] McCune, J. E., and Tavares, T. S., "Perspective: Unsteady Wing Theory–The Kármán/Sears Legacy," *Journal of Fluids Engineering*, Vol. 115, No. 4, 1993, pp. 548–560. https://doi.org/10.1115/1.2910179

[21] Moored, K. W., "Unsteady Three-Dimensional Boundary Element Method for Self-Propelled Bio-Inspired Locomotion," *Computers & Fluids*, Vol. 167, May 2018, pp. 324–340. https://doi.org/10.1016/j.compfluid.2018.03.045

[22] Moored, K. W., and Quinn, D. B., "Inviscid Scaling Laws of a Self-Propelled Pitching Airfoil," *AIAA Journal*, Vol. 57, No. 9, Sept. 2018, pp. 1–15. https://doi.org/10.2514/1.J056634

[23] Floryan, D., Van Buren, T., Rowley, C. W., and Smits, A. J., "Scaling the Propulsive Performance of Heaving and Pitching Foils," *Journal of Fluid Mechanics*, Vol. 822, July 2017, pp. 386–397. https://doi.org/10.1017/jfm.2017.302

[24] Van Buren, T., Floryan, D., and Smits, A. J., "Scaling and Performance of Simultaneously Heaving and Pitching Foils," *AIAA Journal*, Vol. 57, No. 9, Sept. 2019, pp. 1–12. https://doi.org/10.2514/1.J056635

[25] Ayancik, F., Zhong, Q., Quinn, D. B., Brandes, A., Bart-Smith, H., and Moored, K. W., "Scaling Laws for the Propulsive Performance of Three-Dimensional Pitching Propulsors," *Journal of Fluid Mechanics*,

Vol. 871, July 2019, p. 1117–1138.
https://doi.org/10.1017/jfm.2019.334

[26] Ayancik, F., Fish, F. E., and Moored, K. W., "Three-Dimensional Scaling Laws of Cetacean Propulsion Characterize the Hydrodynamic Interplay of Flukes' Shape and Kinematics," *Journal of the Royal Society Interface*, Vol. 17, No. 163, 2020, Paper 20190655.
https://doi.org/10.1098/rsif.2019.0655

[27] Mivehchi, A., Dahl, J., and Licht, S., "Heaving and Pitching Oscillating Foil Propulsion in Ground Effect," *Journal of Fluids and Structures*, Vol. 63, May 2016, pp. 174–187.
https://doi.org/10.1016/j.jfluidstructs.2016.03.007

[28] Van Buren, T., Floryan, D., Wei, N., and Smits, A. J., "Flow Speed has Little Impact on Propulsive Characteristics of Oscillating Foils," *Physical Review Fluids*, Vol. 3, No. 1, 2018, Paper 013103.
https://doi.org/10.1103/PhysRevFluids.3.013103

[29] Saadat, M., Fish, F. E., Domel, A. G., Di Santo, V., Lauder, G. V., and Haj-Hariri, H., "On the Rules for Aquatic Locomotion," *Physical Review Fluids*, Vol. 2, Aug. 2017, Paper 083102.
https://doi.org/10.1103/PhysRevFluids.2.083102

[30] Fish, F. E., "Power Output and Propulsive Efficiency of Swimming Bottlenose Dolphins (Tursiops Truncatus)," *Journal of Experimental Biology*, Vol. 185, Dec. 1993, pp. 179–193.
https://doi.org/10.1242/jeb.185.1.179

[31] Fish, F. E., "Comparative Kinematics and Hydrodynamics of Odontocete Cetaceans: Morphological and Ecological Correlates with Swimming Performance." *Journal of Experimental Biology*, Vol. 201, No. 20, 1998, pp. 2867–2877.
https://doi.org/10.1242/jeb.201.20.2867

[32] Fish, F. E., "Biomechanical Perspective on the Origin of Cetacean Flukes," *The Emergence of Whales*, Springer, Boston, MA, 1998, pp. 303–324.
https://doi.org/10.1007/978-1-4899-0159-0_10

[33] Sambilay, V. C., Jr., "Interrelationships Between Swimming Speed, Caudal Fin Aspect Ratio and Body Length of Fishes," *Fishbyte*, Vol. 8, No. 3, 1990, pp. 16–20.

[34] Krasny, R., "Desingularization of Periodic Vortex Sheet Roll-Up," *Journal of Computational Physics*, Vol. 65, No. 2, 1986, pp. 292–313.
https://doi.org/10.1016/0021-9991(86)90210-X

[35] Fish, F. E., Schreiber, C. M., Moored, K. W., Liu, G., Dong, H., and Bart-Smith, H., "Hydrodynamic Performance of Aquatic Flapping: Efficiency of Underwater Flight in the Manta," *Aerospace*, Vol. 3, No. 3, 2016, p. 20.
https://doi.org/10.3390/aerospace3030020

[36] Akoz, E., and Moored, K. W., "Unsteady Propulsion by an Intermittent Swimming Gait," *Journal of Fluid Mechanics*, Vol. 834, Jan. 2018, pp. 149–172.
https://doi.org/10.1017/jfm.2017.731

[37] Perkins, M., Elles, D., Badlissi, G., Mivehchi, A., Dahl, J., and Licht, S., "Rolling and Pitching Oscillating Foil Propulsion in Ground Effect," *Bioinspiration & Biomimetics*, Vol. 13, No. 1, 2017, Paper 016003.
https://doi.org/10.1088/1748-3190/aa8a12

[38] Prandtl, L., "Theory of Lifting Surfaces," NACA TN 9, 1920, pp. 1–11.

[39] Brennen, C. E., "A Review of Added Mass and Fluid Inertial Forces," Naval Civil Engineering Lab, TR CR 82.010, Sierra Madre, 1982, http://resolver.caltech.edu/CaltechAUTHORS:BREncel82, http://authors.library.caltech.edu/233/ [retrieved 28 Oct. 2015].

[40] Senturk, U., and Smits, A. J., "Reynolds Number Scaling of the Propulsive Performance of a Pitching Airfoil," *AIAA Journal*, Vol. 57, No. 7, 2019, pp. 2663–2669.
https://doi.org/10.2514/1.J058371

[41] Floryan, D., Van Buren, T., and Smits, A. J., "Efficient Cruising for Swimming and Flying Animals is Dictated by Fluid Drag," *Proceedings of the National Academy of Sciences*, Vol. 115, No. 32, 2018, pp. 8116–8118.
https://doi.org/10.1073/pnas.1805941115

[42] Lewin, G. C., and Haj-Hariri, H., "Modelling Thrust Generation of a Two-Dimensional Heaving Airfoil in a Viscous Flow," *Journal of Fluid Mechanics*, Vol. 492, Oct. 2003, pp. 339–362.
https://doi.org/10.1017/S0022112003005743, http://www.journals.cambridge.org/abstract_S0022112003005743 [retrieved 17 July 2020].

[43] Kurt, M., and Moored, K. W., "Flow Interactions of Two- and Three-Dimensional Networked Bio-Inspired Control Elements in an In-Line Arrangement," *Bioinspiration and Biomimetics*, Vol. 13, May 2018, Paper 045002.
https://doi.org/10.1088/1748-3190/aabf4c

[44] Akoz, E., Mivehchi, A., and Moored, K. W., "Intermittent Unsteady Propulsion with a Combined Heaving and Pitching Foil," *Physical Review Fluids*, Vol. 6, No. 4, 2021, pp. 1–21.
https://doi.org/10.1103/PhysRevFluids.6.043101

[45] Anderson, J. M., Streitlien, K., Barrett, D. S., and Triantafyllou, M. S., "Oscillating Foils of High Propulsive Efficiency," *Journal of Fluid Mechanics*, Vol. 360, April 1998, pp. 41–72.
https://doi.org/10.1017/S0022112097008392

H. Dong
Associate Editor